Opt Quant Electron (2008) 40:685–694
DOI 10.1007/s11082-008-9256-z

Optoelectronic conversion of short pulses in sub-micrometer GaAs active devices

M. A. Alsunaidi

Received: 25 June 2008 / Accepted: 15 October 2008 / Published online: 13 November 2008
© Springer Science+Business Media, LLC. 2008

Abstract The accelerating integration of microwave and optical components in modern optoelectronic systems stimulates comprehensive investigations of device operation and efficiency. This paper studies the optoelectronic conversion capabilities of sub-micron GaAs active devices in response to ultra-short illumination pulses. The physical phenomena involved in the photo-electronic effects are appropriately accounted for using a physical device model based on the solution of the Boltzmann's transport equations. The study targets important optical performance indicators including terminal photocurrent peak value and switching time. A figure-of-merit is defined to quantify the overall response. Results show that operating and geometrical conditions can play important roles in the device design, operation and optimization process.

Keywords Optoelectronics · FDTD · Illumination effects · Physical models · Short optical pulses

1 Introduction

Modern high-speed optoelectronic devices and circuits have been improving at a fast pace and there is a growing interest in their integration. Silicon photonics have been realized since the late 1980s by the works of Soref and Petermann (Soref and Lorenzo 1986; Schuppert et al. 1989). In general, silicon photonics is favorable based on its compatibility with the mature silicon IC manufacturing. This fact necessarily leads to low-cost photonics (Jalali and Fathpour 2006). Other advantages of silicon include the availability of high-quality silicon-on-insulator wafers that provide strong optical confinement, an ideal platform for planar waveguides (Jalali et al. 1998). In addition, silicon has excellent material properties such as high thermal conductivity, high optical damage threshold and high third-order optical

M. A. Alsunaidi (✉)
Department of Electrical Engineering, King Fahd University of Petroleum & Minerals, P.O. Box 200, Dhahran 31261, Saudi Arabia
e-mail: msunaidi@kfupm.edu.sa

nonlinearities, which exceed that of the popular III–V counterparts (e.g., GaAs; Jalali et al. 2006). Based on these advantages, several researchers have proposed novel silicon-based photonic devices (Miller 2007).

The overwhelming focus of the scientific community, however, has been on III–V photonics, being the benchmark for all other technologies. The superiority of III–V photonics lies in the following properties. Being direct-gap semiconductors, the radiative lifetime rate is very high. In fact, the radiative process is orders of magnitude faster than any defect or impurity-based nonradiative processes. This fact translates into a conversion efficiency that is close to unity for materials like GaAs (Jalali et al. 2006). The major deficiency in optical conversion in bulk silicon need to overcome the limitations associated with the indirect gap by electron spatial confinement, impurity doping or by using Raman scattering to achieve optical gain (Pavesi and Guillot 2006).

Device modeling for circuit simulation provides an important facility towards linking new device development and its applications. Reliable modeling methods and simulation codes are becoming the basis for the optimizations development of emerging and future optoelectronic devices. Traditionally, GaAs-based optoelectronics industry has relied mainly on experimental optimization—a costly and time-consuming process. Most of the modeling efforts reported in literature on this topic are mainly concerned with the dc and large-signal characterization of illuminated GaAs active devices. These efforts fall in two main categories: analytical and equivalent circuit models. A recent review of these GaAs models can be found in Alsunaidi (2000) and Murty and Jit (2006). Although they provide representations of the device global operating conditions, analytical models are very well known for their simplifying assumptions. On the other hand, equivalent circuit models are very useful in describing the overall functionality of the circuits but do not provide accurate accounts of the physical phenomena. In both modeling techniques, repeated modeling efforts have to be exercised when different regions of device operation or different illumination conditions are considered. Also, the treatment of short-optical-pulse effects into these models is not straightforward. An alternative technique is based on physical models, where the fundamental equations describing the microscopic carrier transport phenomena are solved numerically (Alsunaidi 2000). With this technique, all physical considerations are accommodated and, usually, the same simulation algorithm is used for any geometrical, operational or input conditions.

For microwave and millimetre wave applications, simplified physical simulation models based on the drift-diffusion equations and local field models are not adequate. These models assume that the carrier transport takes place under equilibrium conditions. The Boltzmann's transport equation (BTE), on the other hand, provides time-dependent representations of the carrier density, carrier energy and carrier momentum, and takes care of sub-picosecond non-equilibrium transport. A numerical simulation algorithm based on the finite-difference time-domain (FDTD) method that consistently solves the BTE under illumination conditions has been developed and rigorously validated and tested in several publications (Alsunaidi 2000; Alsunaidi et al. 1997, 2001).

In this paper, a detailed analysis of the effects of biasing, geometry and illumination conditions on typical sub-micrometer gate GaAs active device is presented. The analysis targets two important optical performance factors: terminal photocurrent peak value and discharge time. The two factors represent, respectively, the conversion efficiency and the switching speed of the device. A figure-of-merit is defined to quantify individual effects on the device response. These results should serve as guidelines for device and circuit designers, a valuable reference that is lacking in literature.

2 Device model

In order to describe the illumination effects on the behavior of the active device, accurate modeling of the carrier transport as well as the illumination interaction mechanisms is needed. The carriers in sub-micrometer gate-length devices transport under non-isothermal and non-equilibrium conditions. As a result, appropriate account for the relationship between carrier transport parameters and carrier energy has to be made. Also, the spatial and temporal variations in the carrier momentum cannot be neglected. Short-pulse illumination effects inside the active device should be appropriately included by adequate representation of carrier photo-generation/recombination processes.

The active device model is based on the moments of the BTE obtained by integration over momentum space. The integration results in a strongly-coupled highly-nonlinear set of partial differential equations called the conservation equations (Alsunaidi 2000; Blotekjaer 1970). These equations provide a time-dependent self-consistent solution for carrier density, carrier energy and carrier momentum and are given by

$$\frac{\partial n}{\partial t} + \nabla \cdot (n\nu) = G - R \tag{1}$$

$$\frac{\partial e}{\partial t} + \nu \cdot \nabla e + \frac{1}{n}\nabla \cdot (nk_B T \nu) = -qE \cdot \nu - \frac{e - e_o}{\tau_e} \tag{2}$$

$$\frac{\partial (m\nu_{x,y})}{\partial t} + \nu \cdot \nabla (m\nu_{x,y}) + \frac{q}{n}\frac{\partial}{\partial x, y}(nk_B T) = -qE_{x,y} - \frac{\nu_{x,y}}{\tau_m} \tag{3}$$

where, n is the carrier density, ν is the carrier velocity, e is the carrier energy, E is the electric field intensity, m is the carrier effective mass, T is temperature and τ_e and τ_m are the energy and momentum relaxation times, respectively. The total current density distribution J is given by

$$J(t) = qh(t)\nu_h(t) - qn(t)\nu_e(t) \tag{4}$$

where q is the electronic charge and h and n are the instantaneous hole and electron densities, respectively. The electric potential distribution inside the device is calculated using Poisson's equation as

$$\nabla \cdot [\varepsilon(x, y)\nabla V(x, y)] = -\rho_\nu(x, y) \tag{5}$$

where the permittivity, ε, of each region of the structure is incorporated in the formulation. The free charge density is given by

$$\rho_\nu(x, y) = q\left[N_d^+ - n(x, y) - N_a^- + h(x, y)\right] \tag{6}$$

where N_d and N_a are the ionized donor and acceptor impurity densities, respectively. The model equations are solved in their complete form emphasizing the fact that carrier momentum takes a finite time to adjust itself in response to changes in the electric field. This phenomenon is a distinct feature of high-frequency short gate length devices, which cannot be accounted for in classical drift-diffusion models.

The generation rate, G, is a function of optical intensity, material absorption coefficient and spatial distribution, and is given by

$$G = \phi(x, t)\,\alpha\, e^{-\alpha\, y} \tag{7}$$

where α is the optical absorption coefficient of the material. In Eq. 7, ϕ represents the profile of the incident beam in the transverse direction modulated by a time-domain Gaussian pulse such that

$$\phi(x,t) = \phi_o\, e^{-x^2/\sigma_x^2} e^{-(t-t_o)^2/\sigma_t^2} \tag{8}$$

where ϕ_o is the peak incident power, σ_x is the transverse profile variance and t_o and σ_t are the time-domain pulse peak time and pulse waist, respectively. A number of recombination processes can take place inside the active device such as the Shockley–Read–Hall process and the Auger recombination process (Sze 1981). All of these processes contribute to the recombination rate, R.

The coupling procedure between the two models can be understood by inspecting the physical operations that take place inside the device. The absorbed light creates a disturbance in the carrier distribution inside the device, which in turn results in a change in the current densities. The moving free charges behave as sources of electric fields which alter the carrier velocity and energy. In this fashion, energy coupling between the device and the optical input is established.

3 Results and analysis

The model equations are solved numerically using the FDTD technique. Poisson's equation is solved self-consistently with the BTE device model equations. This procedure is marched in time until transients as well as steady state solutions are achieved. The FDTD formulation is complemented with the definition of appropriate boundary conditions around the simulated structure. The simulated structure consists of a 0.1 μm thick active layer on top of a 1 μm thick substrate to accommodate for the significant amount of carrier injection. A 1 μm thick layer of air is also included on top of the device to account for the fringing fields. The thickness of all electrodes is taken to be 0.2 μm. The spatial step sizes are set as a small fraction of the Debye length to minimize numerical dispersion. Space increments of $\Delta x = 0.025$ μm and $\Delta y = 0.015$ μm are used to adequately represent the smallest dimensions of the device. The numerical algorithm is stable for time steps in the order of 1 fs. The carrier transport parameters (e.g., temperature, mass and relaxation times) are updated each time step, based on the carrier energy.

In order to establish an accurate simulation model that accounts for illumination effects and consequently build confidence in the simulation results, preliminary dc simulations are obtained and verified using available experimental data. The experimental set-up is similar to that used in Kawasaki et al. (1998). Figure 1 shows the structure of the GaAs-based device under study. Also, Table 1 gives the device parameters and operating conditions. Direct illumination is carried out from the top of the device using a semiconductor laser with $\lambda = 820$ nm and a spot diameter of 10 μm. Figure 2 shows representative I–V curves for the dark and illuminated device for $V_{gs} = 0.2$ V. These curves are compared to experimental data as well as values obtained using the equivalent circuit model presented in Kawasaki et al. (1998). The figure shows that the I–V characteristics obtained by the various approaches are in a close agreement. The results obtained by the physical model give, in general, more accurate estimations of device current than the fitting model. As indicated earlier, illumination induces a considerable disturbance in the steady-state carrier distribution inside the device through the carrier generation process and the subsequent high-field transport. The region of high carrier concentration extends well into the substrate as shown in carrier distribution contours of Fig. 3.

Unlike CW optical excitations, the response of the active device under pulsed illumination conditions is characterized by three distinct phases. As shown in Fig. 4, the photocurrent signal registered at the drain side experiences an initial delay. This delay is related to the

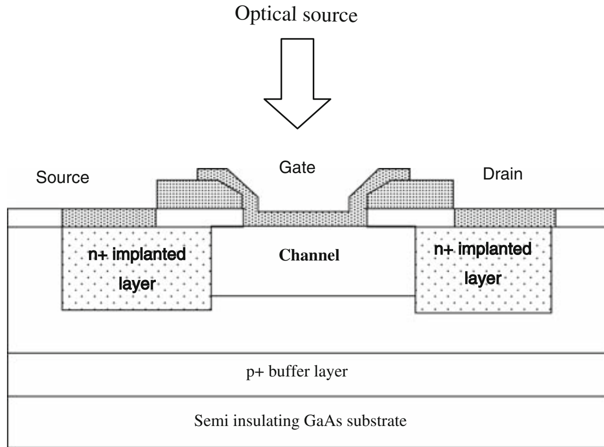

Fig. 1 Structure of the active device used in the analysis

Table 1 Active device parameters

Drain and source contacts (μm)	0.5
Gate length (μm)	0.2
Active layer thickness (μm)	0.1
Active layer doping (cm^{-3})	2×10^{17}
Substrate doping (cm^{-3})	1×10^{14}
Peak optical flux density ($cm^{-2}\,s^{-1}$)	2×10^{21}
Gate-source bias (V)	0.0
Drain-source bias (V)	2.0
Absorption coefficient (cm^{-1})	1×10^{4}

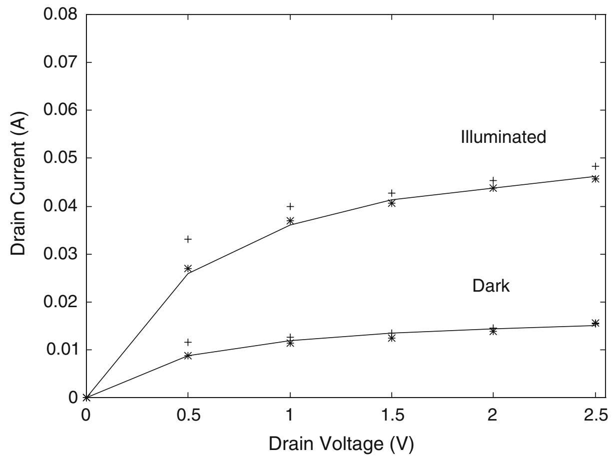

Fig. 2 Representative IV curves of simulated dark and illuminated devices (*solid line*) as compared to experimental values (*) and equivalent circuit model (+)

average electron transit time across the active length of the device. The next phase is the charging phase, where the photocurrent starts to increase as more carriers are generated in response to the illumination pulse and are swept to the output electrodes. The photocurrent

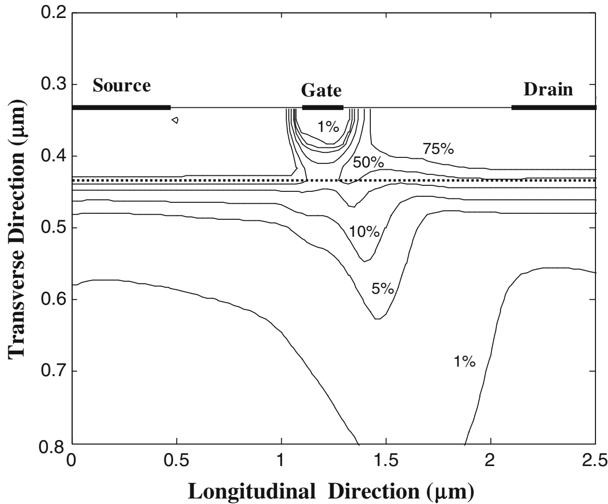

Fig. 3 Electron concentration in the illuminated device. The contour lines represent electron densities given as percentages of the initial active layer doping. The boarder of the active layer is indicated by the *dotted line*. The region of high carrier concentration extends well into the substrate

Fig. 4 Photocurrent generated in response to a 10-ps illumination pulse. For this curve: gate length = 0.2 μm, drain-gate spacing = 0.7 μm, $V_{ds} = 2.0$ V, $V_{gs} = 0.0$ V and peak optical flux density = 2×10^{21} cm^{-2} s^{-1}

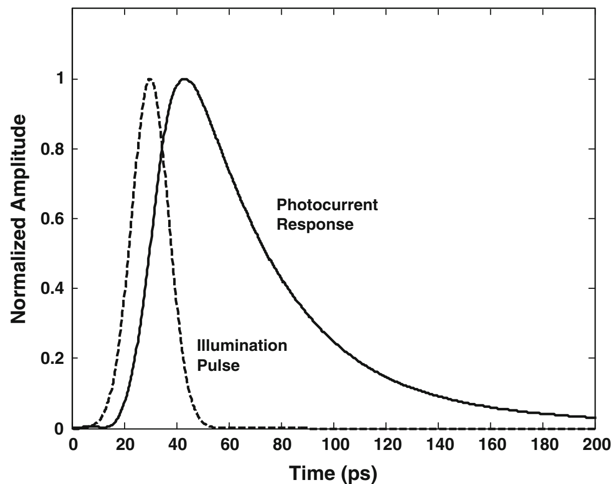

rate of increase, however, is slower than that of the illumination pulse. In fact, the charging rate is proportional to the carrier density inside the device as given by the continuity equation and the overall transport kinetics. Consequently, the photocurrent reaches its peak at a delayed time relative to the peak of the illumination pulse. The third phase, the discharge phase, has a rate governed by the recombination rate and the device intrinsic parameters. In general, the overall response of the device is mainly characterized by the peak photocurrent (conversion efficiency) and the discharge rate (switching speed).

The current investigations are concerned with the pulsed optical response of the illuminated device due to three groups of effects; electrical bias, geometrical variations and optical input conditions. In the first group, the variations in the gate-source and drain-source voltages are independently studied. In the second group, the variations in the device gate length and

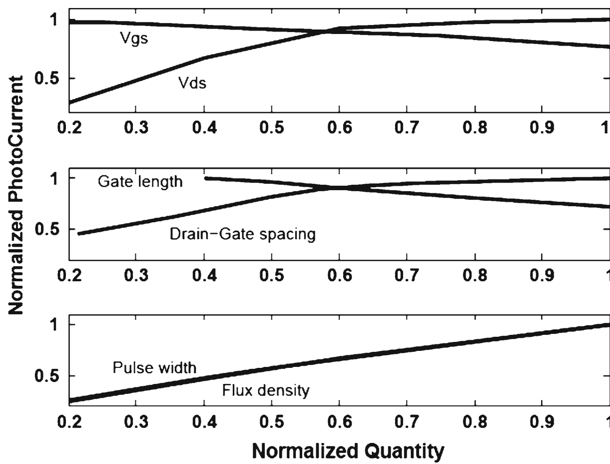

Fig. 5 Effects of electrical bias, device geometry and optical input on output photocurrent. The output photocurrent in the figure is normalized to the maximum value in each case. The normalized x-axis corresponds to the following ranges: V_{gs}: 0 to −0.8 V, V_{ds}: 1–5 V, gate length: 0.2–0.5 µm, drain-gate spacing: 0.3–1.4 µm, optical pulse width: 2–10 ps and optical flux density: 1×10^{21}–20×10^{21} cm^{-2} s^{-1}

drain-gate spacing are considered. Finally, the third group includes the effects of the peak value and duration of the input optical pulse. Each parameter is studied independently of the other parameters. The device is connected in a common-source amplifier configuration and is operated in the saturation region such that amplification of the optical response is attained. The following simulation settings are used as reference values; gate length = 0.2 µm, drain-gate spacing = 0.7µm, active layer thickness = 0.1µm, active layer doping = 2×10^{17} cm^{-3}, V_{ds} = 2.0 V, V_{gs} = 0.0 V, peak optical flux density = 2×10^{21} cm^{-2} s^{-1} and optical pulse width = 10 ps.

Figure 5 shows the variation of peak output photocurrent in response to the three effect groups. The axes of the figure have been normalized such that relative comparisons are readily observable and meaningful. The peak output photocurrent is defined as the maximum value that the pulsed output current reaches in response to the optical input pulse. As shown in the figure, biasing conditions on the gate and drain terminals produce the expected effects. Increasing the negative biasing on the gate limits the effective active layer thickness and the output photocurrent. On the other hand, stronger positive bias on the drain side causes the device to saturate. Time-domain simulations show the significant effect of electrode spacing, specifically, the drain-gate separation, as shown in Fig. 6. On the other hand, the effect of source-gate spacing is less significant (Fig. 7). Whereas longer gate lengths present higher pressure on the active layer and cause the peak output current to drop, the drain-gate separation has an interesting effect. Figure 5 shows that the output photocurrent increases sharply as the separation is increased from 0.3 µm to around 0.8 µm because more device surface is exposed to illumination and more carriers are being generated and transported to the drain by the high field region. However, as the drain-gate separation is increased further, the rate of increase in photocurrent peak value slows down. This behavior is due to the long journey that carriers have to travel to the drain contact and chances of recombination becoming greater. Finally, it is evident from Fig. 5 that the device under study performs better for wider input pulses due to the inherent relaxation times that govern carrier transport.

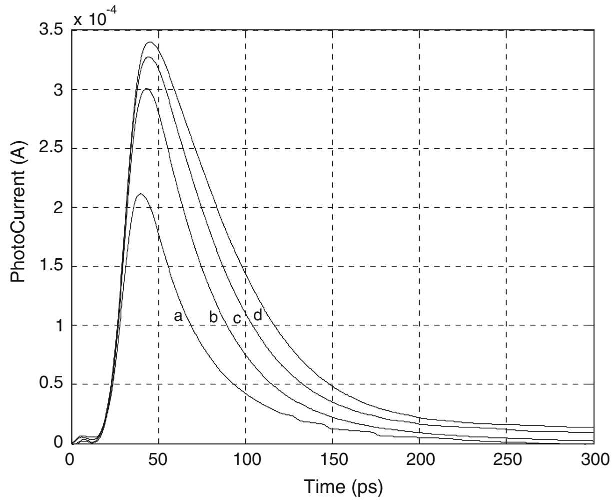

Fig. 6 Photocurrent generated in response to a 20-ps light pulse. The characteristics of the output electronic pulse is a strong function of drain-gate separation (a) 0.5 µm, (b) 0.8 µm, (c) 1.1 µm and (d) 1.4 µm

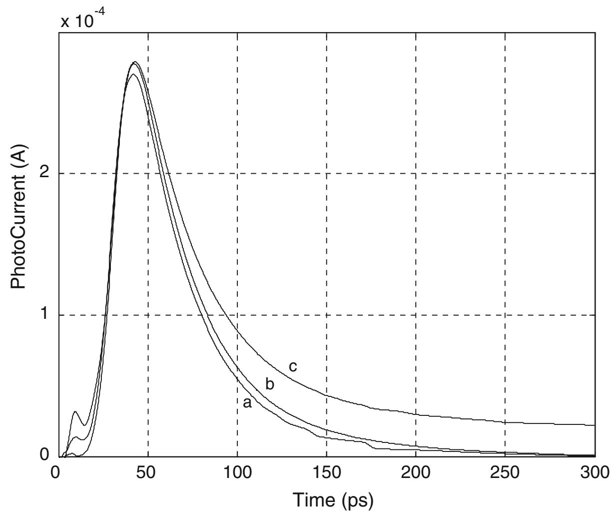

Fig. 7 The effect of source-gate separation (a) 0.3 µm, (b) 0.6 µm and (c) 1.0 µm, on the generated photocurrent with fixed drain-gate separation

Figure 8 shows the device output discharge rate due to the same parameter variations as in Fig. 5. The discharge rate is defined as the time it takes the output photocurrent to drop to $1/e$ of its peak value. Stronger potential differences between the drain and the gate terminals produce higher field regions that accelerate the transport of the carriers to the drain terminal which results in shorter discharge times. This behavior is clearly exhibited when the device gate length or drain-gate spacing is decreased. On the other hand, illumination pulse width does not seem to significantly affect the switching time of the device. Nevertheless, higher flux densities tend to lower the drain-gate potential difference and hence slightly increase the discharge rate.

To quantify a trade-off between conversion efficiency and device switching characteristics, it is important to sum-up the above effects in a single representative quantity. A figure-of-merit can be defined as

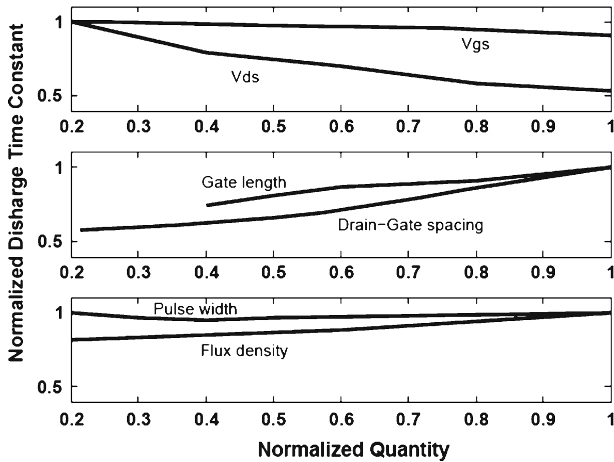

Fig. 8 Effects of electrical bias, device geometry and optical input on output discharge rate. Axes are normalized in the same manner as in Fig. 5

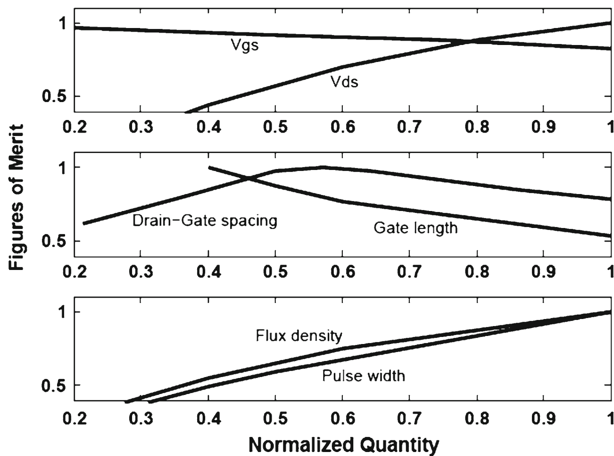

Fig. 9 Figures of merit. Axes are normalized in the same manner as in Fig. 5

$$FoM = \frac{\text{Peak Current Value}}{\text{Discharge Time}} \tag{9}$$

To maintain the highest possible level of optical-to-electrical energy conversion without significantly limiting the device switching speed, the *FoM* has to be maximized. In Fig. 9, the *FoM* is plotted versus all effects in the three groups. The *FoM* values are normalized by the maximum value of each case independently. According to the figure, best performance is expected if the drain bias is made as high as possible with shorter gate length devices. The figure also shows that the drain-gate spacing plays an important role in the device optimization process. Finally, it is apparent that the device under consideration fails to efficiently respond to very short optical pulses. This is an indication that the maximum operating frequency for the device has been exceeded.

4 Conclusions

The effects of operating and geometrical parameters on the pulsed optical response of illuminated active devices have been presented. The FDTD simulations of an energy-based model of carrier transport under illumination conditions were produced and analyzed. The optoelectronic performance of the device in response to a short-pulse illumination has been studied in terms of terminal photocurrent peak and discharge rate. Using a defined figure-of-merit, the simulation results showed that optimum device operation under illumination can be predicted. In particular, electrode spacing plays an important role in device optimization. In the near future, the simulation results will be utilized in the design of an optimum optical communication system with continuous pulse inputs.

Acknowledgment The author would like to acknowledge the support of King Fahd University of Petroleum & Minerals.

References

Alsunaidi, M.A.: Energy model for optically controlled MESFETs. Microw. Opt. Technol. Lett. **26**, 48–52 (2000). doi:10.1002/(SICI)1098-2760(20000705)26:1<48::AID-MOP15>3.0.CO;2-0

Alsunaidi, M.A., Hammadi, S., El-Ghazaly, S.: A parallel implementation of a two-dimensional hydrodynamic model for microwave semiconductor device including inertia effects in momentum relaxation. Int. J. Numer. Model. **10**, 107–119 (1997). doi:10.1002/(SICI)1099-1204(199703)10:2<107::AID-JNM263>3.0.CO;2-F

Alsunaidi, M.A., Kuwayama, T., Kawasaki, S.: Numerical characterization of optically controlled MESFETs using an energy-dependent physical simulation model. IEICE Trans. Electron. **7**, 869–874 (2001)

Blotekjaer, K.: Transport equations for electrons in two-valley semiconductors. IEEE Trans. Electron. Dev. **17**, 38–47 (1970). doi:10.1109/T-ED.1970.16921

Jalali, B., Fathpour, S.: Silicom photonics. J. Lightwave Technol. **24**, 4600–4615 (2006). doi:10.1109/JLT.2006.885782

Jalali, B., Yegnanarayanan, S., Yoon, T., Yoshimoto, T., Rendina, I., Coppinger, F.: Advances in silicon-on-insulator optoelectronics. IEEE J. Sel. Top. Quantum Electron. **4**, 938–947 (1998). doi:10.1109/2944.736081

Jalali, B., Paniccia, M., Reed, G.: Silicom photonics. IEEE Microw. Mag. **7**, 58–68 (2006). doi:10.1109/MMW.2006.1638290

Kawasaki, S., Shiomi, H., Matsugatani, K.: A novel FET model including an illumination intensity parameter for simulation of optically controlled millimeter-wave oscillators. IEEE Trans. Microw. Theory Tech. **46**, 820–828 (1998). doi:10.1109/22.681206

Miller, D.A.: Germanium quantum wells for high-performance modulators in silicon photonics. Photonics Spectra 80–83 (2007)

Murty, N., Jit, S.: A new analytical model for photo-dependent capacitances of GaAs MESFETs with emphasis on the substrate related effects. Solid-State Electron. **50**, 1716–1727 (2006). doi:10.1016/j.sse.2006.09.017

Pavesi, L., Guillot, G.: Optical interconnects: the silicon approach. Springer, New York (2006)

Schuppert, B., Schmidtchen, J., Petermann, K.: Optical channel waveguides in silicon diffused from GeSi alloy. Electron. Lett. **25**, 1500–1502 (1989). doi:10.1049/el:19891007

Soref, R., Lorenzo, J.: All-silicon active and passive guided-wave components for $\lambda = 1.3$ and 1.6 μm. IEEE J. Quantum Electron. **22**, 873–879 (1986). doi:10.1109/JQE.1986.1073057

Sze, S.: Physics of semiconductor devices. Wiley, New York (1981)